AGU PUBLICATIONS

Geophysical Research Letters

RESEARCH LETTER
10.1002/2017GL073943

Key Points:
- New gravity wave data set from the Aeronomy of Ice in the Mesosphere Cloud Imaging and Particle Size satellite instrument
- Near-global coverage at 50–55 km altitude for waves with horizontal wavelength from 15 to 600 km and vertical wavelength longer than 15 km
- New data fill key spatial and temporal gaps in current record and are particularly relevant to vertical propagation of gravity waves

Correspondence to:
C. E. Randall,
cora.randall@colorado.edu

Citation:
Randall, C. E., et al. (2017), New AIM/CIPS global observations of gravity waves near 50–55 km, *Geophys. Res. Lett.*, *44*, 7044–7052, doi:10.1002/2017GL073943.

Received 23 APR 2017
Accepted 22 JUN 2017
Accepted article online 26 JUN 2017
Published online 7 JUL 2017

New AIM/CIPS global observations of gravity waves near 50–55 km

C. E. Randall[1,2], J. Carstens[3], J. A. France[1,4], V. L. Harvey[1], L. Hoffmann[5], S. M. Bailey[3], M. J. Alexander[6], J. D. Lumpe[7], J. Yue[8], B. Thurairajah[3], D. E. Siskind[9], Y. Zhao[10], M. J. Taylor[10], and J. M. Russell III[8]

[1]Laboratory for Atmospheric and Space Physics, University of Colorado Boulder, Boulder, Colorado, USA, [2]Department of Atmospheric and Oceanic Sciences, University of Colorado Boulder, Boulder, Colorado, USA, [3]Center for Space Science and Engineering, Bradley Department of Electrical and Computer Engineering, Virginia Polytechnic Institute and State University, Blacksburg, Virginia, USA, [4]GATS, Inc., Boulder, Colorado, USA, [5]Jülich Supercomputing Centre, Forschungszentrum Jülich, Germany, [6]NorthWest Research Associates, Boulder, Colorado, USA, [7]Computational Physics Inc., Boulder, Colorado, USA, [8]Center for Atmospheric Sciences, Hampton University, Hampton, Virginia, USA, [9]Space Science Division, Naval Research Laboratory, Washington, District of Columbia, USA, [10]Center for Atmospheric and Space Sciences, Utah State University, Logan, Utah, USA

Abstract This paper describes a new data set from the Aeronomy of Ice in the Mesosphere (AIM) Cloud Imaging and Particle Size (CIPS) instrument, from which gravity waves (GWs) at an altitude of 50–55 km can be inferred. CIPS is sensitive to GWs with horizontal wavelengths from ~15 to 600 km and vertical wavelengths longer than 15 km. Several examples of GWs in CIPS observations are shown, including waves associated with the Andes Mountains, island topography, convection, the polar night jet, and the tropospheric jet stream. GW signatures in the CIPS data are shown to agree well with near-coincident but lower altitude measurements from the Atmospheric Infrared Sounder (AIRS) in June of 2016. Results suggest the power of combining CIPS measurements with those from other instruments to investigate GW filtering and propagation. The CIPS data set opens new areas of inquiry, enabling comprehensive investigations of GWs in the middle atmosphere on a near-global scale.

Plain Language Summary This paper describes a new data set from the Cloud Imaging and Particle Size instrument on the NASA Aeronomy of Ice in the Mesosphere satellite. The data set can be used to infer atmospheric gravity waves at an altitude of 50-55 km. Several examples of gravity waves are shown, including waves associated with the Andes Mountains, island topography, convection, the polar night jet, and the tropospheric jet stream. Gravity wave signatures in the new data set are shown to agree well with near-coincident but lower altitude measurements from the satellite-based Atmospheric Infrared Sounder. Results suggest the power of combining the new data with measurements from other instruments to investigate gravity wave filtering and vertical propagation. This data set opens new areas of inquiry, enabling comprehensive investigations of gravity waves in the middle atmosphere on a near-global scale. Such studies are important because gravity waves drive the circulation in the middle and upper atmosphere, thereby impacting global atmospheric structure, composition, and variability.

1. Introduction

Vertically propagating gravity waves (GWs) play a significant role in coupling the atmosphere, as they transfer momentum and energy from the troposphere to higher altitudes. They drive the residual circulation in the upper atmosphere [*Lindzen*, 1981; *Holton*, 1982, 1983], thereby impacting global atmospheric structure, composition, and variability. Among other important ramifications, GWs influence the dynamical and chemical structure of the Antarctic polar vortex [*Garcia et al.*, 2017], modulate the atmospheric response to Arctic stratospheric sudden warmings [*Ern et al.*, 2016], trigger the formation of polar stratospheric clouds [*Cariolle et al.*, 1989; *Hoffmann et al.*, 2017], and modulate polar mesospheric cloud occurrence [*Gerrard et al.*, 2004].

GWs act on subgrid scales in global climate models and therefore must be parameterized. Improving these parameterizations is an active area of research and requires observations of GW effects on a global scale throughout the lower and middle atmosphere [*Alexander et al.*, 2010; *Fritts and Alexander*, 2003; *Geller et al.*, 2013]. Numerous instruments have been used in recent years to study GWs [*Alexander et al.*, 2010;

Wright et al., 2016a, 2016b]. Because the data from different instruments pertain to different spatial, spectral, and temporal scales [e.g., *Alexander and Barnet*, 2007], a complete understanding of GWs requires that the various observations be combined. Near-global, satellite-based limb sounders such as the Sounding of the Atmosphere using Broadband Emission Radiometry (SABER) [*Alexander et al.*, 2015; *Ern et al.*, 2016; *Geller et al.*, 2013; *Preusse et al.*, 2009], Cryogenic Infrared Spectrometers and Telescopes for the Atmosphere (CRISTA) [*Eckermann and Preusse*, 1999; *Preusse et al.*, 2002], and Microwave Limb Sounder (MLS) [*Jiang et al.*, 2002; *Wright et al.*, 2016b] have broad vertical coverage but lack horizontal imaging capability. Nadir sounders such as the Atmospheric Infrared Sounder (AIRS) [*Gong et al.*, 2015; *Hoffmann and Alexander*, 2009] and the Visible Infrared Imaging Radiometer Suite (VIIRS) [*Miller et al.*, 2015] have extensive horizontal coverage, but vertical weighting functions that limit vertical resolution and range.

This paper reports a new, near-global, nadir-imaging data set that can be used to infer GWs near an altitude of 50–55 km. To our knowledge, this is the only available imaging data set that can reveal horizontal GW structures near the stratopause. The measurements are made by the Cloud Imaging and Particle Size (CIPS) instrument on the NASA Aeronomy of Ice in the Mesosphere (AIM) satellite [*Russell et al.*, 2009]. The new CIPS data complement the AIRS measurements, which are widely used for GW studies but have limited utility above ~40 km [*Wright et al.*, 2016a]. They also complement the VIIRS measurements and CIPS inferences of GWs from polar mesospheric cloud (PMC) images [*Chandran et al.*, 2010; *Yue et al.*, 2014; *Zhao et al.*, 2015], both near altitudes of 80–90 km.

2. Instruments and Retrieval Algorithm

AIM was launched in April 2007 and is still operational. CIPS is a nadir-viewing panoramic imager that measures ultraviolet radiation scattered by the clouds and atmosphere [*McClintock et al.*, 2009; *Rusch et al.*, 2009]. It was designed to image the atmosphere over a wide range of scattering angles, with a primary goal of measuring PMCs [*Bailey et al.*, 2009]. The instrument consists of four cameras operating in a 10 nm passband centered at 265 nm, with a total cross-track by along-track field of view of 80° × 120° (~1000 km × 2000 km), centered at the subsatellite point. Individual camera pixels have a horizontal resolution of 1 km × 2 km in the nadir, but the data are binned to 7.5 km × 7.5 km in the retrieval process to approximately match the poorer horizontal resolution at the highest viewing angles. CIPS images are acquired simultaneously in each camera, with the combined four-camera image being referred to as a "scene."

From launch in 2007 until February of 2016, CIPS scenes were acquired every 43 s in the spring or summer hemisphere between the terminator and a dayside latitude of ~40°. With this cadence, many locations were viewed at as many as seven different scattering angles, which provided a direct measurement of the scattering phase function. The radiance observed by CIPS comes from molecular (Rayleigh) scattering by the background atmosphere, as well as from ice particle scattering by PMCs, if present. The CIPS version 4.20 PMC retrieval algorithm relies on the premise that PMCs can be distinguished from the background Rayleigh scattering by their asymmetric phase function, as described by *Lumpe et al.* [2013]. CIPS PMC retrievals based on this scattering angle approach were validated by *Benze et al.* [2009, 2011], confirming that CIPS measurements of scattered radiance are reliable. Furthermore, as noted by *Carstens et al.* [2013], a Rayleigh scattering model based on *McPeters* [1980] and modified for the CIPS observing geometry [*Bailey et al.*, 2009] matched the background albedo measured by CIPS to within 2%.

The robust quality of CIPS Rayleigh scattering measurements has enabled production of the new data described in this paper. In the absence of PMCs, the Rayleigh scattering source function for the 265 nm radiance observed by CIPS peaks near an altitude of 50–55 km [*Bailey et al.*, 2009]. Since the observed Rayleigh scattering signal is controlled by the atmospheric neutral density and is modulated strongly by ozone absorption [*Bailey et al.*, 2009; *McPeters*, 1980], coherent perturbations to the observed Rayleigh scattering signal on scales of tens to hundreds of kilometers are generally indicative of GW-induced variations in the neutral density and/or ozone near 50–55 km. To quantify these perturbations, we calculate the Rayleigh Albedo Anomaly (RAA), which is defined as the residual difference between the observed Rayleigh scattering albedo and a "baseline" albedo that would be observed in the absence of any small-scale atmospheric variations.

In theory, the baseline albedo could be calculated by smoothing the observed albedo to average out perturbations. Because each CIPS pixel is characterized by a unique observation geometry, however, such a smoothing is not feasible in practice. Instead, the baseline albedo is calculated using a numerical

generalization of the "*C*-σ" model [e.g., *Carstens et al.*, 2013]. Details of the RAA retrieval will be given elsewhere. Briefly, the process begins with calculation of the level 1 observed albedo, *R*, as described in *Lumpe et al.* [2013]. For each 7.5 km × 7.5 km RAA bin, or resolution element, *R* can be expressed as the product of two terms:

$$R = R_n(N_{O3}, N_{tot}, \sigma) \times G(\theta, \mathrm{VWA}, \mathrm{SZA}, \sigma) \quad (1)$$

Here *G* is a geometric factor for the RAA bin that depends on the scattering angle (θ), view angle (VWA, the angle between the local zenith and the CIPS line of sight to the scattering volume), solar zenith angle (SZA), and the ratio of the ozone scale height to the atmospheric scale height near 50–55 km (σ); note that VWA and SZA vary along the line of sight. All parameters in *G* except for σ are known for every RAA bin. The RAA retrieval assumes monthly mean climatological values for σ in 10° latitude bins as calculated by *McPeters and Labow* [2012] from MLS ozone. Geophysical variability in σ, as observed by MLS, is insignificant for the purposes of the CIPS retrievals, justifying the use of climatological data. R_n is the Rayleigh albedo that would be observed at $\theta = 90°$ and VWA = 0° and is essentially a scaling factor on the Rayleigh scattering phase function. R_n depends on σ as well as N_{O3} and N_{tot}, the ozone and atmospheric column densities, respectively, above the peak of the Rayleigh scattering source function. With an assumed value of σ, *G* is known, so R_n can be calculated for each RAA bin as *R*/*G*. The R_n values on each day are then fitted via bilinear interpolation to a smooth, continuous surface defined by vertices on a 10° latitude by 20° longitude grid. The optimal surface is solved for iteratively for each day of observations by minimizing the total root-mean-square difference between all R_n values and the surface. The final surface evaluated at each bin location defines the baseline albedo, R_{base}, so that the final RAA in each bin, expressed as a percent, is given by

$$\mathrm{RAA} = 100\ (R_n - R_{base})/R_{base} \quad (2)$$

PMCs interfere with the RAA retrieval, so RAA data are most robust in their absence. As noted above, until February of 2016, CIPS measurements spanned latitudes from ~40° to the pole in the spring or summer hemisphere. Thus, RAA data for those years are restricted to latitudes of ~40°N–90°N from March equinox to September equinox, and from ~40°S to 90°S from September equinox to March equinox, except during the PMC seasons (~June–August in the north and December–February in the south), when the PMC region is excluded. In February of 2016 CIPS switched into a continuous imaging mode of operations, wherein images are acquired every 3 min throughout the sunlit portion of the orbit. Therefore, the RAA data since February of 2016 are global in the sunlit hemisphere except near the summer pole during the PMC seasons. Dictated by the RAA bin size and CIPS scene size, the RAA retrievals are most sensitive to perturbations from GWs with horizontal wavelengths of ~15–600 km; detection of longer-wavelength GWs is possible but requires that the wave crests be aligned along track or nearly so. The RAA retrievals are most sensitive to GWs with vertical wavelengths ≥15 km, which is determined by the vertical weighting function for the ozone absorption contribution to the observed albedo.

The next section describes comparisons between CIPS RAA and AIRS Brightness Temperature Perturbation (BTP) data. Details of the AIRS instrument and BTP retrievals have been given elsewhere [*Hoffmann et al.*, 2014, and references therein]. Briefly, contributions to the total brightness temperature (BT) variance measured by AIRS come from atmospheric temperature variations associated primarily with large-scale features such as latitude gradients and planetary waves, and smaller-scale features such as GWs. The AIRS BTP retrieval removes the larger-scale deviations by calculating a fourth-order polynomial fit to the BT measurements in the cross-track direction for each scan. Subtraction of this fit from the measured BT yields the BTP, which is thus a measure of small-scale deviations from the smooth background. Therefore, the AIRS BTP data product is analogous to the CIPS RAA data product, in that both are measures of small-scale perturbations to the background atmosphere that are usually attributed to GWs.

We use the 4.3 μm AIRS data, for which the spectral mean vertical weighting function maximizes around an altitude of 30–40 km. *Hoffmann et al.* [2014] show that the sensitivity of the 4.3 μm BTP variance data exceeds 50% for GWs with vertical wavelengths longer than ~65 km, although GWs with vertical wavelengths as short as ~15 km are detectable. The sensitivity exceeds 50% for horizontal wavelengths ranging from ~100 to 1000 km. Sensitivity to GWs with shorter wavelengths is restricted by the AIRS horizontal footprint, which has a nadir diameter of 13.5 km and increases to 39.6 km at the largest viewing angles [*Sato et al.*, 2016].

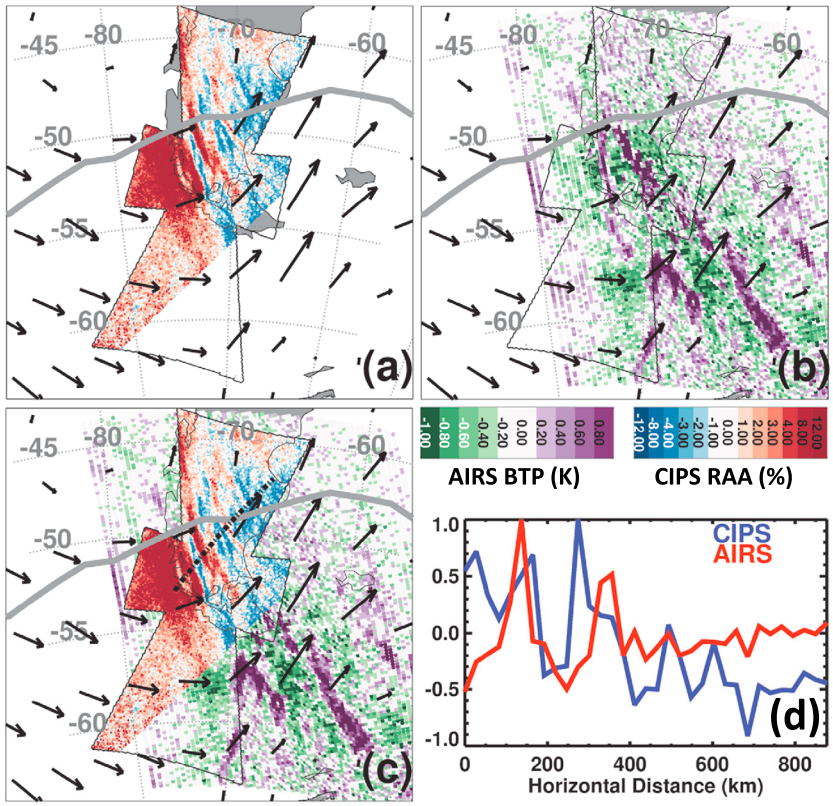

Figure 1. (a) CIPS RAA in a single four-camera scene and (b) AIRS 4.3 μm BTP, over the tip of South America on 10 June 2016, with the outline of the CIPS scene superimposed. (c) CIPS scene superimposed on AIRS. Arrows show MERRA-2 horizontal winds at 850 hPa interpolated to the CIPS time; wind velocities were constant within several m/s throughout the previous 24 h (not shown). In accordance with the higher CIPS spatial resolution, each AIRS data point here and in Figure 2 occupies an area equal to 4 times the area of each CIPS data point. In Figures 1a–1c thick gray curves indicate the edge of the Antarctic vortex at a potential temperature of 1600 K (~45 km) [*Harvey et al.,* 2002]; numbers refer to latitudes (45°S–60°S) and longitudes (60°W–80°W). (d) Normalized CIPS RAA and AIRS BTP, taken perpendicular to the GW fronts along the dash-dotted line in Figure 1c.

The average footprint diameter is ~20 km [*Alexander and Teitelbaum*, 2011], suggesting that the minimum horizontal wavelength detectable in AIRS data is typically ~40 km, more than twice as long as the minimum horizontal wavelength detected by CIPS.

3. Results and Discussion

Figure 1 compares CIPS RAA data in one four-camera scene to AIRS BTP data over the tip of South America on 10 June 2016. The CIPS scene was acquired at 20:04 UT; the AIRS data were acquired earlier from 18:35 UT to 18:41 UT. The bowtie-shaped, black outline denotes the edges of the CIPS scene; data are missing in the lower right part of the scene because of proximity to the terminator, where radiances are too low for robust measurements. The CIPS RAA values in Figures 1 and 2 exhibit systematic trends in the cross-track (approximately longitudinal) dimension because the baseline albedo calculation does not yet completely account for SZA changes across the scene; this does not significantly impact the results reported here, which focus on the superimposed smaller-scale variations. The wavelike features seen in both the CIPS and AIRS data sets are typical of stratospheric GW signatures previously reported in the literature [e.g., *Hoffmann and Alexander*, 2009]. The superimposed 850 hPa (~1.5 km altitude) wind vectors in Figures 1a–1c were derived from the Modern-Era Retrospective analysis for Research and Applications, version 2 (MERRA-2) [*Bosilovich et al.*, 2015]; wind speeds were ~20 m/s in the region of the wave features observed by CIPS. The southern Andes region is a well-known source of orographic GWs [*Hoffmann et al.*, 2016], and orographic generation is consistent with the high tropospheric wind speeds and the fact that the wind vectors are nearly perpendicular to the wavefronts and mountain ridges.

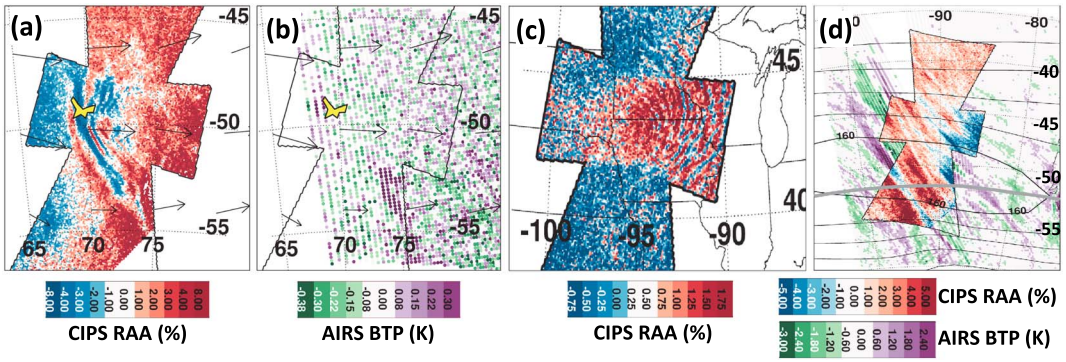

Figure 2. Examples of CIPS RAA and AIRS BTP data on 10–11 June 2016. (a) CIPS RAA at 10:31 UT and (b) AIRS BTP at 8:43–8:49 UT, on 10 June over the Kerguélen Islands (yellow) in the southern Indian Ocean; arrows show MERRA-2 horizontal wind vectors at 850 hPa (1.5 km altitude), interpolated to the CIPS time. (c) CIPS RAA at 22:49 UT on 10 June over the northern midwestern United States. (d) CIPS RAA at 21:28 UT and near-coincident AIRS BTP on 11 June 2016; the AIRS data were acquired on two different orbits, at ~19:23 UT (mainly east of the CIPS scene) and ~21:00 UT (mainly west of the CIPS scene). In Figure 2d the thick gray curve indicates the vortex edge at a potential temperature level of 2000 K (~50 km); black contour lines show the westerly wind speed at 50 km, in increments of 20 m/s, with a maximum of 160 m/s.

The larger-scale GW signatures in CIPS and AIRS data in Figure 1 have similar orientations and horizontal wavelengths. Normalized CIPS RAA and AIRS BTP values along the 875 km transect that is drawn perpendicular to the wavefronts in Figure 1c are shown in Figure 1d. The two prominent crests in the AIRS data are located ~150 km and ~350 km from the zero position (left endpoint of the transect), and the two most prominent troughs in the CIPS data are located ~200 km and ~400 km from the endpoint. Both suggest a horizontal wavelength of ~200 km over the Andes. The observation of similar wave signatures in these near-coincident measurements is consistent with transmission of quasi-stationary, orographically generated waves from the troposphere to the mesosphere [e.g., *Smith et al.*, 2009].

Northeast of the ~200 km wave features, CIPS data exhibit wave patterns with wavelengths closer to ~100 km, which are not seen by AIRS. It is possible that the amplitude and/or vertical wavelength of the waves detected by CIPS were smaller at the lower AIRS observation altitude than AIRS was able to detect [e.g., *Yue et al.*, 2013]. The complex wave features in the CIPS scene may have been generated by a combination of orographic and jet imbalance processes. The gray curve superimposed on the images indicates the edge of the Antarctic polar vortex at 45 km, where winds (not shown) were parallel to the vortex edge and normal to the Andes and varied from 70 to 100 m/s over the CIPS scene. GWs are commonly associated with the winter polar vortex at lower altitudes in the stratosphere [e.g., *Alexander et al.*, 2009; *Plougonven and Zhang*, 2014; *Sato and Yoshiki*, 2008].

Figure 2 shows more examples of GWs, on 10–11 June 2016. Figures 2a and 2b compare CIPS RAA and AIRS BTP on 10 June 2016 near the Kerguélen Islands in the Southern Indian Ocean, another hot spot for orographic GWs [*Hoffmann et al.*, 2016]. The AIRS data were acquired ~105 min before the spatially coincident CIPS scene. CIPS data show signatures of GWs with horizontal wavelengths ranging from ~100 km on the western edge of the islands to ≤40 km downwind of the islands. For reference, the Kerguélen Islands are ~130 km wide from east to west, with mountains that reach 1850 m in height. AIRS data hint at the presence of a wavefront near 55°S/75°E, but the smaller-scale waves downwind of the islands are not evident in the AIRS data. This is probably because the horizontal wavelengths are relatively short, and the GWs in this instance are located near the western edge of the AIRS orbit strip where the horizontal resolution is poorest and signals are smeared [*Gong et al.*, 2012]. This example is important since the cumulative effect of GWs from isolated islands in the Southern Ocean could be significant for the circulation of the middle and upper atmosphere. *Alexander and Grimsdell* [2013] showed that GWs generated by flow over southern ocean island topography are very common in May–September, while *Pautet et al.* [2016] and *Eckermann et al.* [2016] showed that such orographically generated GWs penetrate into the upper mesosphere during winter. Because island GWs can occur frequently, *Alexander and Grimsdell* [2013] concluded that a lack of GW signatures in the AIRS data might often imply that the GWs had dissipated and imparted their momentum in the atmosphere below 40 km. The new availability of CIPS GW measurements at ~50–55 km altitude can be used

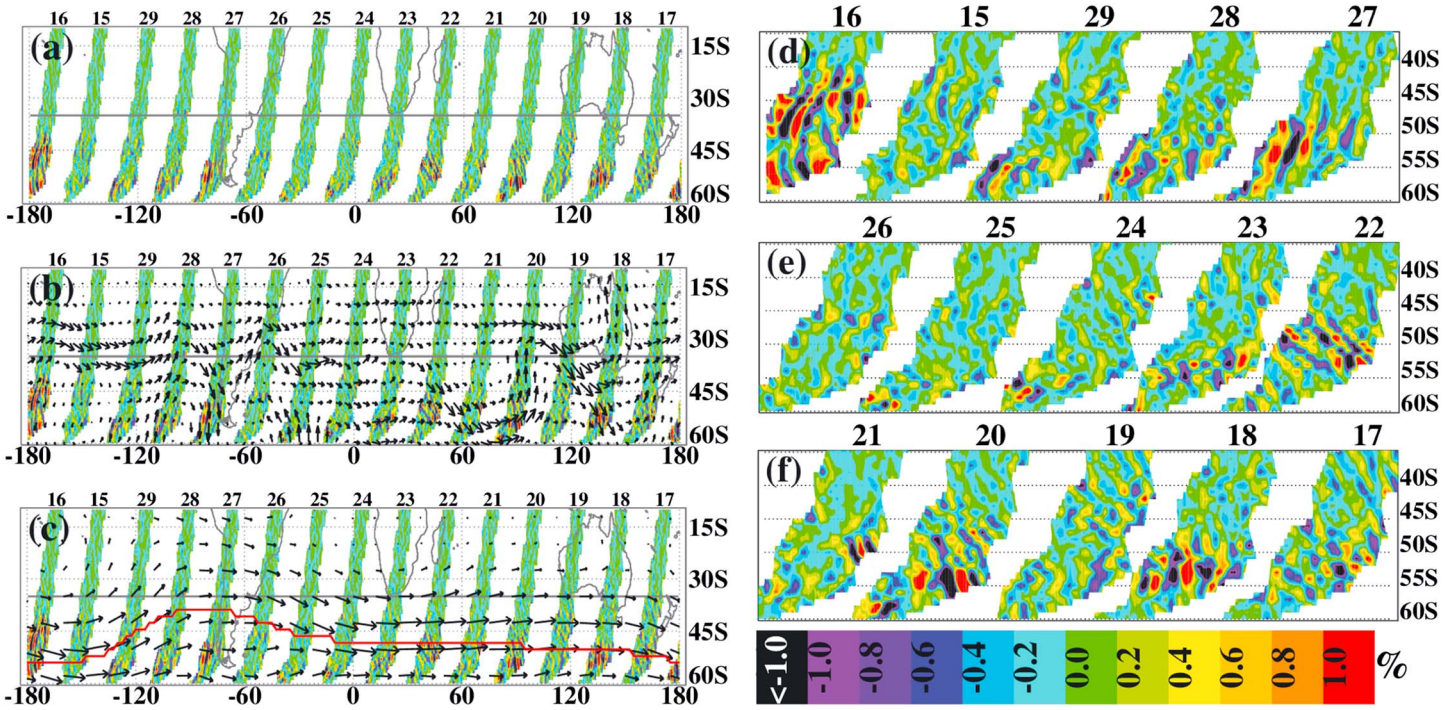

Figure 3. (a–c) CIPS m-RAA (see text) in the latitude range 10°S–60°S, from orbits 50415–50429 on 16 July 2016; the last two digits of the orbit number are given above each orbit strip. Arrows in Figures 3b and 3c denote MERRA-2 wind vectors at 300 hPa and 1 hPa, respectively. The red contour in Figure 3c indicates the vortex edge at a potential temperature level of 2000 K (~1 hPa). (d–f) Expanded view of the m-RAA in Figures 3a–3c poleward of 35°S (marked by the gray line). The orbits have been placed arbitrarily closer to each other in longitude to allow for the expanded view.

effectively with AIRS observations to better quantify the frequency with which island-generated GWs propagate up through the stratosphere and into the mesosphere.

Figures 2c and 2d illustrate nonorographic GWs. Figure 2c shows a partial concentric wave pattern in CIPS RAA data over the northern midwestern United States on 10 June 2016, which exhibits a well-defined center and a horizontal wavelength of ~35–40 km. Such patterns are characteristic of freely propagating, convectively generated GWs [e.g., *Taylor and Hapgood*, 1988, *Yue et al.*, 2014]. The CIPS scene in Figure 2c was acquired at 22:49 UT. An infrared Geostationary Operational Environmental Satellite (GOES) image taken 4 min earlier at 22:45 UT (not shown) indicated strong convective activity that extended from northern Iowa and southern Minnesota through northern Wisconsin and into Canada. The NOAA Storm Prediction Center recorded numerous reports of high winds and hail greater than 5 cm. in diameter across the same region. This example is similar to that depicted in Figure 1 of *Gong et al.* [2015], which showed a partial concentric GW pattern in AIRS data that was associated with an extended convective region in the midwestern U.S. on 26 July 2012. However, the GWs in that case exhibited a much longer horizontal wavelength than the CIPS GWs in Figure 2c. The closest AIRS data (not shown) that covered the geographic region sampled by CIPS on 10 June 2016 were acquired more than 3.5 h earlier and did not show any indication of the concentric GWs. Figure 2d shows CIPS RAA and AIRS BTP data on 11 June 2016. The measurements are located over the South Pacific, west of South America, and indicate excellent agreement between AIRS and CIPS for this nonorographic wave in the stratospheric polar night jet. Note also that the CIPS scene location was near a jet streak at the tropopause (not shown), indicating a possible wave source.

Figure 3 illustrates qualitatively the rich content of CIPS RAA winter hemisphere observations on 16 July 2016. This day was chosen arbitrarily to represent a typical day of measurements. The previous figures showed individual CIPS scenes; Figure 3 shows the results of combining the scenes into orbit strips, each of which is composed of ~15 scenes on the sunlit side of the orbit. In addition, Figure 3 shows a modified RAA (m-RAA), for which large-scale longitudinal variations were removed to better isolate GW signatures in the longitudinal direction. Specifically, the CIPS RAA data were averaged into 1° latitude by 0.1° longitude bins. In each latitude bin, a smooth background was calculated as a running boxcar average of the RAA over

~3° in longitude and subtracted from the RAA. A 1° (in longitude) running boxcar average was then applied to the residual, to produce the m-RAA shown in Figure 3. The boxcar sizes were chosen empirically to optimally represent wave patterns without substantially damping their amplitude.

As seen in Figures 3a–3c, every orbit on this day shows GW signatures, most of which occurred at middle to high latitudes. The waves were inside, outside, and on the edge of the polar vortex, and often near topographic features. Figures 3d–3f give expanded views of each orbit to illustrate more clearly the GWs. The largest wave patterns are in orbit 50416, from 40°S to 60°S, near the Date Line and east-southeast of New Zealand, a known hot spot for GW generation. Recent analyses of data from the DEEPWAVE campaign suggest that GWs observed in the upper stratosphere and lower mesosphere near New Zealand are likely generated by both orographic and nonorographic sources and also raise the question of what controls the propagation of GWs into the upper mesosphere [*Fritts et al.*, 2016]. One of the surprising findings of DEEPWAVE was the transmission to the mesosphere of mountain waves with horizontal wavelengths of ~10–30 km; since CIPS is sensitive to GWs with λ as small as 15 km, the RAA data will be invaluable in investigations of these waves. The largest GW signals in orbit 50421 are in the vicinity of the Kerguélen Islands and are likely orographic in origin.

It is likely that many of the GWs depicted in Figure 3 are nonorographic. Wind vectors based on MERRA-2 data at 300 hPa (approximate level of the tropospheric jet) and 1 hPa are given in Figures 3b and 3c. The large m-RAA wave patterns in orbit 50427 are located just west of the southern tip of South America, where tropospheric winds rule out an orographic origin. The GWs near 55°S on orbit 50420 are located near the exit region of a jet streak at 300 hPa, which *Zhang* [2004] showed could generate GWs; although it is also possible that the GWs in orbit 50420 are associated with leeward propagation of orographic GWs generated over the Kerguélen Islands, as discussed by *Preusse et al.* [2002] and *Sato et al.* [2012]. Many of the other strong wave signatures, such as those poleward of 45°S in orbits 50418, 50428, and 50429, are relatively distant from land masses. The CIPS data could therefore lead to an improved understanding of nonorographic wave sources.

4. Summary

This paper presents a new data set from the AIM CIPS instrument, from which GWs near the stratopause can be inferred. Examples described herein include both orographic and nonorographic GWs, and waves that were most likely associated with island topography, convection, and tropospheric jet stream sources. These examples demonstrate that the AIM CIPS RAA data provide an important new measurement capability for scientific investigations of GW activity. CIPS measurements are sensitive to waves near 50–55 km altitude with horizontal wavelengths of ~15–600 km, and vertical wavelengths $\geq$15 km. As such, the AIM CIPS instrument occupies a unique niche, filling in spatial and temporal gaps in the current measurement record, and providing information that is particularly relevant to the vertical propagation of GWs.

At the time of this writing, near-global CIPS RAA data are available from March 2016 to February 2017, except in the PMC regions and from 6 August 2016 to 15 October 2016 when CIPS turned off temporarily for spacecraft purposes. The RAA algorithm is also being applied to ongoing measurements, which are near global. RAA data from 2007 to 2015 will be made available after they are processed and will consist of measurements in the summer hemisphere poleward of ~40°, minus the PMC region. By combining CIPS data with measurements from other instruments, GWs can be observed independently at multiple altitudes. Observing the change in GW spectrum with altitude can help to constrain and validate the GW parameterizations used in general circulation models [*Alexander et al.*, 2010]. Such studies will be instrumental in clarifying the impact of stratospheric variability on GW propagation. For example, GW events seen in AIRS but not in CIPS might demonstrate significant wave filtering or breaking below the stratopause. Comprehensive examination of CIPS data in conjunction with other GW data sets, simultaneous temperature and wind information from reanalysis data such as MERRA-2, and 3-D ray tracing programs will elucidate the propagation of GWs from the troposphere up through the middle atmosphere.

Acknowledgments
CIPS RAA data and read software are available to the community via download from http://lasp.colorado.edu/aim. AIRS data are distributed by the NASA Goddard Earth Sciences Data Information and Services Center. MERRA-2 data are provided by the Global Modeling and Assimilation Office at NASA Goddard Space Flight Center. AIM is funded by the NASA Small Explorer program. We thank the AIM operations and CIPS ground data system teams for excellent support.

References

Alexander, M. J., and C. Barnet (2007), Using satellite observations to constrain parameterizations of gravity wave effects for global models, *J. Atmos. Sci.*, *64*, 1652–1665, doi:10.1175/JAS3897.1.

Alexander, M. J., and A. W. Grimsdell (2013), Seasonal cycle of orographic gravity wave occurrence above small islands in the Southern Hemisphere: Implications for effects on the general circulation, *J. Geophys. Res. Atmos.*, *118*, 11,589–11,599, doi:10.1002/2013JD020526.

Alexander, M. J., and H. Teitelbaum (2011), Three-dimensional properties of Andes mountain waves observed by satellite: A case study, *J. Geophys. Res.*, *116*, D23110, doi:10.1029/2011JD016151.

Alexander, M. J., et al. (2010), Recent developments in gravity-wave effects in climate models and the global distribution of gravity-wave momentum flux from observations and models. *Q. J. R. Meteorol. Soc.*, *136*, 1103–1124. doi:10.1002/qj.637.

Alexander, P., A. de la Torre, T. Schmidt, P. Llamedo, and R. Hierro (2015), Limb sounders tracking topographic gravity wave activity from the stratosphere to the ionosphere around midlatitude Andes, *J. Geophys. Res. Space Physics*, *120*, 9014–9022, doi:10.1002/2015JA021409.

Alexander, S. P., A. R. Klekociuk, and T. Tsuda (2009), Gravity wave and orographic wave activity observed around the Antarctic and Arctic stratospheric vortices by the COSMIC GPS-RO satellite constellation, *J. Geophys. Res.*, *114*, D17103, doi:10.1029/2009JD011851.

Bailey, S. M., G. E. Thomas, D. W. Rusch, A. W. Merkel, C. D. Jeppesen, J. N. Carstens, C. E. Randall, W. W. McClintock, and J. M. Russell III (2009), Phase functions of polar mesospheric cloud ice as observed by the CIPS instrument on the AIM satellite, *J. Atmos. Sol. Terr. Phys.*, *71*, 373–380, doi:10.1016/j.jastp.2008.09.039.

Benze, S., C. E. Randall, M. T. DeLand, G. E. Thomas, D. W. Rusch, S. M. Bailey, J. M. Russell III, W. McClintock, A. W. Merkel, C. Jeppesen (2009), Comparison of polar mesospheric cloud measurements from the Cloud Imaging and Particle Size experiment and the solar backscatter ultraviolet instrument in 2007, *J. Atmos. Sol. Terr. Phys.*, *71*, 365–372, doi:10.1016/j.jastp.2008.07.014.

Benze, S., C. E. Randall, M. T. DeLand, G. E. Thomas, S. M. Bailey, J. M. Russell III, and A. W. Merkel (2011), Evaluation of AIM CIPS measurements of polar mesospheric clouds by comparison with SBUV data, *J. Atmos. Sol. Terr. Phys.*, doi:10.1016/j.jastp.2011.02.003.

Bosilovich, M., et al. (2015), MERRA-2: Initial evaluation of the climate, NASA Tech. Rep. Series on Global Modeling and Data Assimilation, NASA/TM–2015-104606, vol. 43.

Cariolle, D., S. Muller, F. Cayla, and M. P. McCormick (1989), Mountain waves, polar stratospheric clouds, and the ozone depletion over Antarctica, *J. Geophys. Res.*, *94*, 11,233–11,240, doi:10.1029/JD094iD09p11233.

Carstens, J. N., S. M. Bailey, J. D. Lumpe, and C. E. Randall (2013), Understanding uncertainties in the retrieval of polar mesospheric clouds from the cloud imaging and particle size experiment in the presence of a bright Rayleigh background, *J. Atmos. Sol. Terr. Phys.*, *104*, 197–212, doi:10.1016/j.jastp.2013.08.006.

Chandran, A., D. W. Rusch, A. W. Merkel, S. E. Palo, G. E. Thomas, S. M. Bailey, and J. M. Russell III (2010), Polar mesospheric cloud structures observed from the cloud imaging and particle size experiment on the Aeronomy of Ice in the Mesosphere spacecraft: Atmospheric gravity waves as drivers for longitudinal variability in polar mesospheric cloud occurrence, *J. Geophys. Res.*, *115*, D13102, doi:10.1029/2009JD013185.

Eckermann, S. D., D. Broutman, J. Ma, J. D. Doyle, P.-D. Pautet, M. J. Taylor, K. Bossert, B. P. Williams, D. C. Fritts, and R. B. Smith (2016), Dynamics of orographic gravity waves observed in the mesosphere over Auckland Islands during the Deep Propagating Gravity Wave Experiment (DEEPWAVE), *J. Atmos. Sci.*, doi:10.1175/JAS-D-16-0059.1.

Eckermann, S. D., and P. Preusse (1999), Global measurements of stratospheric mountain waves from space, *Science*, *286*, 1534–1537, doi:10.1126/science.286.5444.1534..

Ern, M., et al. (2016), Satellite observations of middle atmosphere gravity wave absolute momentum flux and of its vertical gradient during recent stratospheric warmings, *Atmos. Chem. Phys. 16*, 9983–10019, doi:10.5194/acp-16-9983-2016.

Fritts, D. C., and M. J. Alexander (2003), Gravity wave dynamics and effects in the middle atmosphere, *Rev. Geophys.*, *41*(1), 1003, doi:10.1029/2001RG000106

Fritts, D. C., et al. (2016), The Deep Propagating Gravity Wave Experiment (DEEPWAVE): An airborne and groundbased exploration of gravity wave propagation and effects from their sources throughout the lower and middle atmosphere. *Bull. Am. Meteorol. Soc.*, *97*, 425–453, doi:10.1175/BAMS-D-14-00269.1.

Garcia, R. R., A. K. Smith, D. E. Kinnison, A. de la Camara, and D. J. Murphy (2017), Modification of the gravity wave parameterization in the Whole Atmosphere Community Climate Model: Motivation and results, *J. Atmos. Sci.*, *74*, 275–291, doi:10.1175/JAS-D-16-0104.1.

Geller, M. A., M. J. Alexander, P. T. Love, J. Bacmeister, M. Ern, A. Hertzog, E. Manzini, P. Preusse, K. Sato, A. A. Scaife, and T. Zhou (2013), A comparison between gravity wave momentum fluxes in observations and climate models, *J. Clim.*, *26*, 6383–6405, doi:10.1175/JCLI-D-12-00545.1.

Gerrard, A. J., T. J. Kane, S. D. Eckermann and J. P. Thayer (2004), Gravity waves and mesospheric clouds in the summer middle atmosphere: A comparison of lidar measurements and ray modeling of gravity waves over Sondrestrom, Greenland, *J. Geophys. Res.*, *109*, D10103, doi:10.1029/2002JD002783.

Gong, J., D. L. Wu, and S. D. Eckermann (2012), Gravity wave variances and propagation derived from AIRS radiances, *Atmos. Chem. Phys.*, *12*, 1701–1720, doi:10.5194/acp-12-1701-2012.

Gong, J., J. Yue, and D. L. Wu (2015), Global survey of concentric gravity waves in AIRS images and ECMWF analysis, *J. Geophys. Res. Atmos.*, *120*, 2210–2228, doi:10.1002/2014JD022527.

Harvey, V. L., R. B. Pierce, T. D. Fairlie, and M. H. Hitchman (2002), A climatology of stratospheric polar vortices and anticyclones, *J. Geophys. Res.*, *107*(D20), 4442, doi:10.1029/2001JD001471.

Hoffmann, L., and M. J. Alexander (2009), Retrieval of stratospheric temperatures from Atmospheric Infrared Sounder radiance measurements for gravity wave studies, *J. Geophys. Res.*, *114*, D07105, doi:10.1029/2008JD011241.

Hoffmann, L., M. J. Alexander, C. Clerbaux, A. W. Grimsdell, C. I. Meyer, T. Robler, and B. Tournier (2014), Intercomparison of stratospheric gravity wave observations with AIRS and IASI, *Atmos. Meas. Tech.*, *7*, 4517–4537, doi:10.5194/amt-7-4517-2014.

Hoffmann, L., A. W. Grimsdell, and M. J. Alexander (2016), Stratospheric gravity waves at southern hemisphere orographic hotspots: 2003-2014 AIRS/Aqua observations, *Atmos. Chem. Phys.*, *16*, 9381–9397, doi:10.5194/acp-16-9381-2016.

Hoffmann, L., R. Spang, A. Orr, M. J. Alexander, L. A. Holt, and O. Stein (2017), A decadal satellite record of gravity wave activity in the lower stratosphere to study polar stratospheric cloud formation, *Atmos. Chem. Phys.*, *17*, 2901–2920, doi:10.5194/acp-17-2901-2017.

Holton, J. R. (1982), The role of gravity wave induced drag and diffusion in the momentum budget of the mesosphere. *J. Atmos. Sci.*, *39*, 791–799.

Holton, J. R. (1983), The influence of gravity wave breaking on the general circulation of the middle atmosphere, *J. Atmos. Sci.*, *40*, 2497–2507.

Jiang, J. H., D. L. Wu, and S. D. Eckermann (2002), Upper Atmosphere Research Satellite (UARS) MLS observations of mountain waves over the Andes, *J. Geophys. Res.*, *107*(D20), 8273, doi:10.1029/2002JD002091.

Lindzen, R. S. (1981), Turbulence and stress owing to gravity wave and tidal breakdown, *J. Geophys. Res.*, *86*(C10), 9707–9714.

Lumpe, J. D., et al. (2013), Retrieval of polar mesospheric cloud properties from CIPS: Algorithm description, error analysis and cloud detection sensitivity, *J. Atmos. Sol. Terr. Phys.*, *104*, 167–196, doi:10.1016/j.jastp.2013.06.007.

McClintock, W. E., D. W. Rusch, G. E. Thomas, A. W. Merkel, M. R. Lankton, V. A. Drake, S. M. Bailey, and J. M. Russell III (2009), The cloud imaging and particle size experiment on the aeronomy of ice in the mesosphere mission: Instrument concept, design, calibration, and on-orbit performance, *J. Atmos. Sol. Terr. Phys.*, *71*, 340–355.

McPeters, R. D. (1980), The behavior of ozone near the stratopause from two years of BUV observation, *J. Geophys. Res.*, *85*, 4545–4550, doi:10.1029/JC085iC08p04545.

McPeters, R. D., and G. J. Labow (2012), Climatology 2011: An MLS and sonde derived ozone climatology for satellite retrieval algorithms, *J. Geophys. Res.*, *117*, D10303, doi:10.1029/2011JD017006.

Miller, S. D., W. C. Straka III, J. Yue, S. M. Smith, M. J. Alexander, L. Hoffmann, M. Setvak, and P. T. Partain (2015), Upper atmospheric gravity wave details revealed in nightglow satellite imagery, *Proc. Natl. Acad. Sci.*, E6728–E6735, doi:10.1073/pnas.1508084112.

Pautet, P.-D., M. J. Taylor, D. C. Fritts, K. Bossert, B. P. Williams, D. Broutman, J. Ma, S. Eckermann, and J. Doyle (2016), Large amplitude mesospheric response to an orographic wave generated over the Southern Ocean Auckland Islands (50.7°S) during the DEEPWAVE project, *J. Geophys. Res. Atmos.*, *121*, 1431–1441, doi:10.1002/2015JD024336.

Plougonven, R., and F. Zhang (2014), Internal gravity waves from atmospheric jets and fronts, *Rev. Geophys.*, *52*, 33–76, doi:10.1002/2012RG000419.

Preusse, P., A. Dörnbrack, S. D. Eckermann, M. Riese, B. Schaeler, J. Bacmeister, D. Broutman, and K. U. Grossmann (2002), Space based measurements of stratospheric mountain waves by CRISTA: 1. Sensitivity, analysis method and a case study, *J. Geophys. Res.*, *107*(D23), 8178, doi:10.1029/2001JD000699.

Preusse, P., S. D. Eckermann, M. Ern, J. Oberheide, R. H. Picard, R. G. Roble, M. Riese, J. M. Russell III, and M. G. Mlynczak (2009), Global ray tracing simulations of the SABER gravity wave climatology, *J. Geophys. Res.*, *114*, D08126, doi:10.1029/2008JD011214.

Rusch, D. W., G. E. Thomas, W. McClintock, A. W. Merkel, S. M. Bailey, J. M. Russell III, C. E. Randall, C. Jeppesen, and M. Callan (2009), The cloud imaging and particle size experiment on the aeronomy of ice in the mesosphere mission: Cloud morphology for the northern 2007 season, *J. Atmos. Sol. Terr. Phys.*, *71*, 356–364, doi:10.1016/j.jastp.2008.11.005.

Russell, J. M., III et al. (2009), Aeronomy of Ice in the Mesosphere (AIM): Overview and early science results, *J. Atmos. Sol. Terr. Phys.*, *71*, 289–299, doi:10.1016/j.jastp.2008.08.011.

Sato, K., and M. Yoshiki (2008), Gravity wave generation around the polar vortex in the stratosphere revealed by 3-hourly radiosonde observations at Syowa station, *J. Atmos. Sci.*, *65*, 3719–3735, doi:10.1175/2008JAS2539.1.

Sato, K., S. Tateno, S. Watanabe, and Y. Kawatani (2012), Gravity wave characteristics in the southern hemisphere revealed by a high-resolution middle-atmosphere general circulation model, *J. Atmos. Sci.*, *69*, 1378–1396, doi:10.1175/JAS-D-11-0101.1.

Sato, K., C. Tsuchiya, M. J. Alexander, and L. Hoffmann (2016), Climatology and ENSO-related interannual variability of gravity waves in the Southern Hemisphere subtropical stratosphere revealed by high-resolution AIRS observations, *J. Geophys. Res. Atmos.*, *121*, 7622–7640, doi:10.1002/2015JD024462.

Smith, S., J. Baumgardner, and M. Mendillo (2009), Evidence of mesospheric gravity-waves generated by orographic forcing in the troposphere, *Geophys. Res. Lett.*, *36*, L08807, doi:10.1029/2008GL036936.

Taylor, M. J., and M. A. Hapgood (1988), Identification of a thunderstorm as a source of short period gravity waves in the upper atmospheric nightglow emissions, *Planet. Space Sci.*, *36*, 975.

Wright, C. J., N. P. Hindley, A. C. Moss, and N. J. Mitchell (2016a), Multi-instrument gravity-wave measurements over Tierra del Fuego and the Drake Passage—Part 1: Potential energies and vertical wavelengths from AIRS, COSMIC, HIRDLS, MLS-Aura, SAAMER, SABER and radiosondes, *Atmos. Meas. Tech.*, *9*, 877–908, doi:10.5194/amt-9-877-2016.

Wright, C. J., N. P. Hindley, and N. J. Mitchell (2016b), Combining AIRS and MLS observations for three-dimensional gravity wave measurement, *Geophys. Res. Lett.*, *43*, 884–893, doi:10.1002/2015GL067233.

Yue, J., L. Hoffmann, and M. J. Alexander (2013), Simultaneous observations of convective gravity waves from a ground-based airglow imager and the AIRS satellite experiment, *J. Geophys. Res. Atmos.*, *118*, 3178–3191, doi:10.1002/jgrd.50341.

Yue, J., B. Thurairajah, L. Hoffmann, M. J. Alexander, A. Chandran, M. J. Taylor, J. M. Russell III, C. E. Randall, and S. M. Bailey (2014), Concentric gravity waves in polar mesospheric clouds from the Cloud Imaging and Particle Size experiment, *J. Geophys. Res. Atmos.*, *119*, 5115–5127, doi:10.1002/2013JD021385.

Zhang, F. (2004), Generation of mesoscale gravity waves in upper-tropospheric jet-front systems, *J. Atmos. Sci.*, *61*, 440–457.

Zhao, Y., M. J. Taylor, C. E. Randall, J. D. Lumpe, D. E. Siskind, S. M. Bailey, and J. M. Russell III (2015), Investigating seasonal gravity wave activity in the summer polar mesosphere, *J. Atmos. Sol. Terr. Phys.*, *127*, 8–20, doi:10.1016/j.jastp.2015.03.008.